Volume 13
Number 5
7 February 2022
Pages 1181–1514

Chemical Science

rsc.li/chemical-science

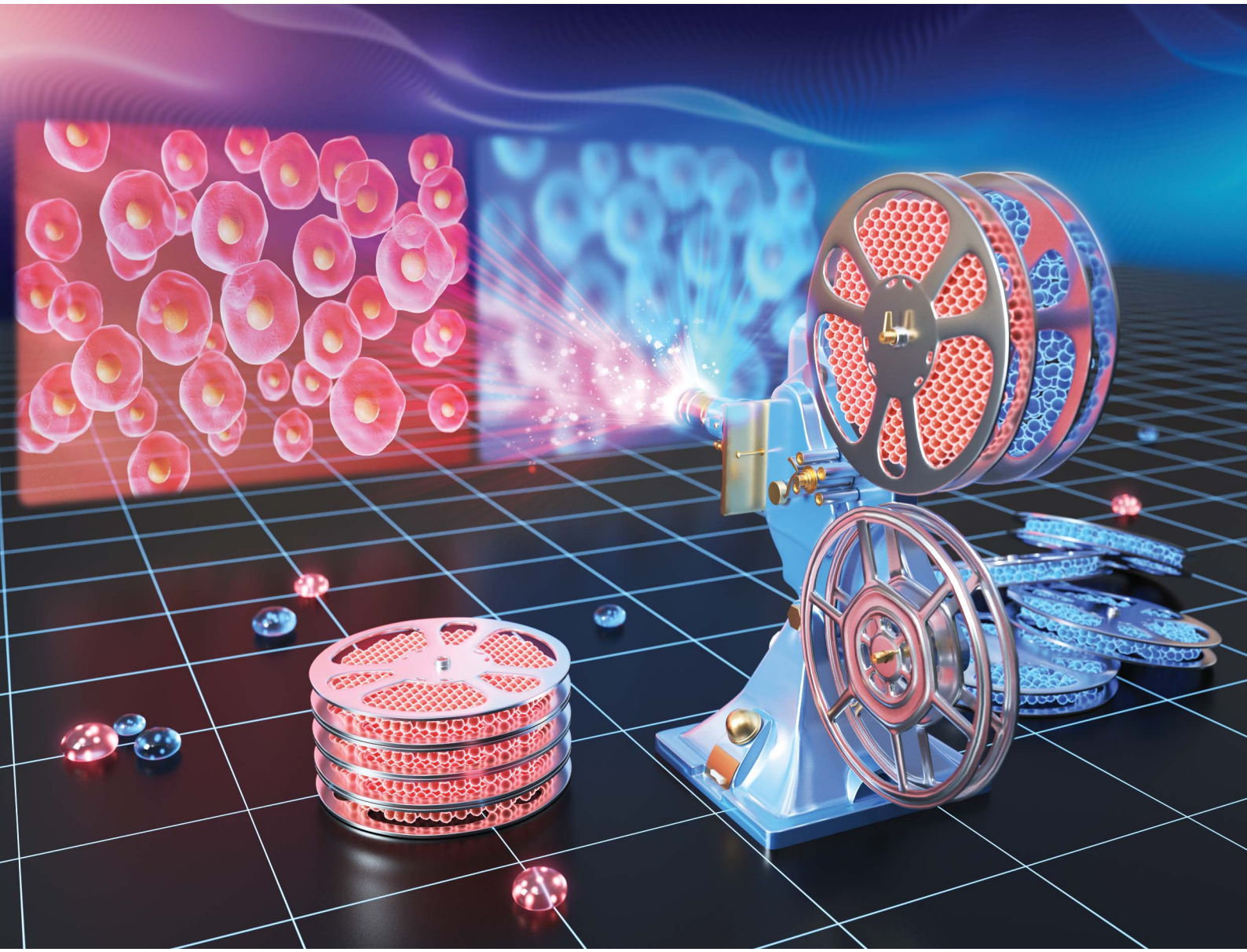

ISSN 2041-6539

ROYAL SOCIETY OF CHEMISTRY

EDGE ARTICLE

Dongfeng Dang, Lingjie Meng *et al.*
Facilely prepared aggregation-induced emission (AIE) nanocrystals with deep-red emission for super-resolution imaging

Chemical Science

ROYAL SOCIETY OF CHEMISTRY

EDGE ARTICLE

View Article Online
View Journal | View Issue

Cite this: *Chem. Sci.*, 2022, **13**, 1270

All publication charges for this article have been paid for by the Royal Society of Chemistry

Facilely prepared aggregation-induced emission (AIE) nanocrystals with deep-red emission for super-resolution imaging†

Ruohan Xu,[a] Dongfeng Dang, *[a] Zhi Wang,[a] Yu Zhou,[bc] Yanzi Xu,[a] Yizhen Zhao,[b] Xiaochi Wang,[a] Zhiwei Yang[b] and Lingjie Meng*[ac]

Received 4th August 2021
Accepted 11th December 2021

DOI: 10.1039/d1sc04254h

rsc.li/chemical-science

Organic nanocrystals (NCs) with high brightness are highly desirable for biological imaging. However, the preparation of NCs by a facile and fast method is still challenging. Herein, an aggregation-induced emission (AIE) luminogen of 4,4′-(5,6-difluorobenzo[*c*][1,2,5]thiadiazole-4,7-diyl)bis(*N*,*N*-bis(4-methoxyphenyl)aniline) (DTPA-BT-F) in the deep-red region is designed with intensive crystalline features to obtain NCs by kinetically controlled nanoprecipitation. The prepared AIE NCs with high brightness and good photo-stability are then applied in super-resolution imaging *via* stimulated emission depletion (STED) nanoscopy. As observed, the nanostructures in lysosomes of both fixed and live cells are well visualized with superior lateral resolutions under STED nanoscopy (full width at half maximum values, 107 and 108 nm) in contrast to that in confocal imaging (548 and 740 nm). More importantly, dynamic monitoring and long-term tracking of lysosomal movements in live HeLa cells, such as lysosomal contact, can also be carried out by using DTPA-BT-F NCs at a superior resolution. To the best of our knowledge, this is the first case of AIE NCs prepared by nanoprecipitation for STED nanoscopy, thus providing a new strategy to develop high performance imaging agents for super-resolution imaging.

Introduction

Over the past few decades, fluorescence microscopy has been widely used in biomedical research for its merits of non-invasiveness, high sensitivity and real-time and *in situ* workability.[1–3] In particular, super-resolution microscopy (SRM) techniques, such as stimulated emission depletion (STED) nanoscopy,[4,5] structured illumination microscopy (SIM),[6,7] and stochastic optical reconstruction microscopy (STORM),[8,9] breaking the optical diffraction limits in conventional microscopy, have served as powerful tools for visualizing nanoscale cellular structures and dynamic monitoring in biological research.[10,11] It is noted that fluorescent probes absolutely play important roles in super-resolution imaging. For instance, fluorophores with high brightness, good photo-stability and high depletion efficiency are desirable for STED nanoscopy.[12,13] Recently, many inorganic fluorophores, including up-conversion nanoparticles (UCNPs)[14] and inorganic quantum dots (QDs),[15] have been demonstrated to be capable for STED super-resolution imaging. Besides, some organic fluorophores with fine-tuned chemical structures, highly emissive features, large Stokes' shifts and excellent biocompatibility, have also attracted increasing interests in this field, indicating their great potential in super-resolution imaging *via* STED nanoscopy.[16–21]

For the commonly used organic fluorophores in STED imaging, the following issues should be well considered: one is the easily occurring photo-bleaching under an intense depletion laser, and the other is inferior emission in aggregates caused by an "aggregation-caused quenching (ACQ)" effect. These two issues seriously limited the signal-to-noise ratios in super-resolution imaging and prevented their applications in long-term tracking at a superior resolution. To solve these problems, organic fluorophores were encapsulated in some polymer matrixes and functionalized as fluorescent nanoparticles (NPs), leading to an enhanced water dispersibility and photo-stability.[22] On the other hand, organic fluorophores with "aggregation-induced emission (AIE)" features were also prepared and used as efficient STED imaging agents due to their highly emissive characteristics in aggregates and impressive photo-stability.[23,24] According to the two considerations, AIE NPs or AIE dots could provide the chance to well meet the requirements in STED nanoscopy.[22,25–28] However, it should be mentioned that for AIE dots, although intramolecular motions can be restricted to some extent, kinetically controlled nanoprecipitation usually produced amorphous particles. Disordered structures in amorphous AIE dots may still suffer from

[a]*School of Chemistry, Xi'an Key Laboratory of Sustainable Energy Material Chemistry, Xi'an Jiao Tong University, Xi'an, 710049, P. R. China. E-mail: dongfengdang@xjtu.edu.cn; menglingjie@xjtu.edu.cn*

[b]*School of Physics, Xi'an Jiao Tong University, Xi'an, 710049, P. R. China*

[c]*Instrumental Analysis Center, Xi'an Jiao Tong University, Xi'an, 710049, P. R. China*

† Electronic supplementary information (ESI) available. See DOI: 10.1039/d1sc04254h

loose molecular packing, allowing free intramolecular motions, and finally resulting in non-radiative decay and limited emission intensity. From this point, there is still large room for the improvement of AIE dots to achieve high performance in super-resolution imaging.

Encouragingly, nano-crystallization was proposed recently to align the molecular packing and further restrain intramolecular motions in AIEgens.[29–33] As a result, the prepared nanocrystals (NCs) could provide significantly enhanced brightness. For example, Zhao, Tang and Liu *et al.* firstly developed a stress-induced seed assisted crystallization method to produce uniform AIE NCs with an appropriate size and much bright emission, which were finally applied in biomedical imaging.[29] Later, by fine-tuning the solvent ratios and storage time for DCCN, Qian and Tang *et al.* also fabricated organic NCs with bright near-infrared emission.[31] These prepared AIE-based NCs indicated great potential in third-harmonic generation (THG) imaging with high spatial resolutions, thus well visualizing the small vessels even at a depth of 800 μm in the mouse brain. In addition, the vortex fluidic device (VFD) method was also employed to prepare NCs by Tang and his co-workers.[32] Through the regulation of water fractions and rotation speed, VFD-mediated NCs having bright emission and narrowed size distribution can be finally obtained. More recently, Wang and Tang *et al.* developed a novel strategy of "photo-induced crystallization with emission enhancement (PICEE)", which was also utilized to form NCs *in situ*.[33] Nevertheless, despite these achievements for nanocrystals, more efforts are still needed for developing highly emissive and uniform NCs in a much fast and facile way. Moreover, the prepared NCs for super-resolution imaging have not been reported yet.

Therefore, in this paper, we firstly prepared highly emissive AIE NCs by a facile nanoprecipitation method by tuning their non-covalent intermolecular actions and achieved their applications in super-resolution imaging *via* STED nanoscopy. To enhance the non-covalent intermolecular interactions, a donor–acceptor-structured AIEgen of DTPA-BT-F with fluorine atoms in the molecular backbone was prepared here, where DTPA-BT-H and DTPA-BT-MO as the contrast were also synthesized. Benefitting from the efficient intramolecular charge transfer (ICT) effect, all these molecules displayed deep-red emission from 550 to 850 nm. Among them, DTPA-BT-F attached with fluorine atoms exhibited an impressive crystalline ability and high brightness in aggregated states (photoluminescence quantum yield, PLQYs = 36.49%). Owing to the significantly enhanced non-covalent interactions, DTPA-BT-F-based nanocrystals (DTPA-BT-F NCs) with uniform size (~50 nm, PDI = 0.21), good stability and also favourable luminescence performance can be well prepared through a facile and fast nanoprecipitation method. Additionally, large Stokes' shift (175 nm; 5668 cm^{-1}), excellent biocompatibility, and high photobleaching resistance even under continuous irradiation of the 775 nm STED beam (600 mW, 25 min) were also observed in DTPA-BT-F NCs. Finally, the prepared NCs were used to stain HeLa cells for super-resolution imaging. It was observed that the nanostructures in lysosomes can be well outlined in both fixed cells and live cells with superior lateral resolutions and much decreased full width at half maximum (FWHM) values of only 107 and 108 nm under STED nanoscopy, which is much better than that in confocal microscopy (548 and 740 nm). More importantly, 3D reconstructed STED imaging and dynamic monitoring of lysosomal movements in live HeLa cells by using DTPA-BT-F NCs were also realized with high spatial resolution due to their outstanding photo-stability and high depletion efficiency. To the best of our knowledge, this is the first case of AIE NCs prepared by nanoprecipitation for STED nanoscopy, which may provide a new strategy to enrich the toolbox of high performance imaging agents in super-resolution imaging.

Results and discussion

To produce D–A type 4,4′-(benzo[*c*][1,2,5]thiadiazole-4,7-diyl) bis(*N*,*N*-bis(4-methoxyphenyl)aniline) (DTPA-BT-H), 4,4′-(5,6-dimethoxybenzo[*c*][1,2,5]thiadiazole-4,7-diyl)bis(*N*,*N*-bis(4-methoxyphenyl)aniline) (DTPA-BT-MO) and 4,4′-(5,6-difluorobenzo[*c*][1,2,5]thiadiazole-4,7-diyl)bis(*N*,*N*-bis(4-methoxyphenyl)aniline) (DTPA-BT-F) (Fig. 1A), electron-donating triphenylamine (TPA) units and electron-withdrawing benzothiadiazole (BT) cores grafted with different side groups, such as hydrogen atoms, methoxy groups and fluorine atoms, were employed, and their synthetic routes are displayed in the ESI (Scheme S1†). The chemical structures were well characterized (Fig. S1–S9, ESI†). All the prepared molecules exhibited good solubility in common solvents, such as tetrahydrofuran (THF). Firstly, UV-vis absorption and photoluminescence (PL) spectra of DTPA-BT-H, DTPA-BT-MO and DTPA-BT-F in dilute THF solution ($[c] = 1 \times 10^{-5}$ M) were recorded. As shown in Fig. 1B, due to the charge transfer

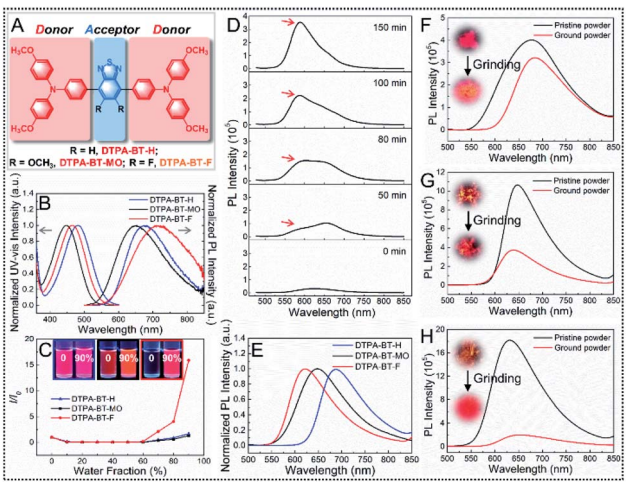

Fig. 1 Chemical structures of DTPA-BT-H, DTPA-BT-MO and DTPA-BT-F (A) and their normalized UV-vis/PL spectra in THF (B); plots of I/I_0 values for DTPA-BT-H, DTPA-BT-MO and DTPA-BT-F in THF/water mixtures with different f_w (C, the insets show the images of three compounds at f_w = 0 and 90% under UV light irradiation); time-dependent fluorescence spectra of DTPA-BT-F in the THF/water mixture at f_w = 60% (D); normalized PL spectra of DTPA-BT-H, DTPA-BT-MO and DTPA-BT-F in solids (E); their PL intensity profiles, and corresponding fluorescent powders before and after grinding (F–H).

between TPA and BT units in the molecular backbones, these compounds displayed typical ICT absorption peaked at 481, 448 and 465 nm, respectively.[34] In contrast to DTPA-BT-H, the absorption was blue-shifted for both DTPA-BT-MO and DTPA-BT-F due to the steric hindrance of the methoxy group and fluorine atom.[35,36] Besides, all these molecules exhibited high molar extinction coefficients (ε), where that of DTPA-BT-F even reached 5.19×10^4 M^{-1} cm^{-1} (Fig. S10, ESI†). On the other hand, all these molecules showed deep red/NIR emission in THF solution in the range of 550–850 nm, but it is noted that red-shifted emission with decreased signals occurred in DTPA-BT-F in contrast to DTPA-BT-H and DTPA-BT-MO. This is probably caused by the strong twisted intramolecular charge transfer (TICT) effect due to the electron-withdrawing ability of the fluorine atom in DTPA-BT-F. Additionally, mega Stokes' shifts of up to ~200 nm (~6000 cm^{-1}) in developed molecules and even of 254 nm (7597 cm^{-1}) in DTPA-BT-F were observed here (Table S1, ESI†). This is quite favorable for avoiding auto-fluorescence interference and can also reduce the re-excitation process by the STED beam.[12,37] Then, UV-vis absorption and PL spectra of DTPA-BT-H, DTPA-BT-MO and DTPA-BT-F in solvents with varied polarities were studied (Fig. S11, ESI†), and the corresponding Lippert–Mataga plots were also obtained (Fig. S12, ESI†). As we anticipated, red-shifted emission can be found in all the molecules when increasing the solvent polarity from hexane to dimethyl sulfoxide (DMSO), especially in the case of DTPA-BT-F, further suggesting its strong TICT effect in polar media.[38]

To study the AIE characteristics of DTPA-BT-H, DTPA-BT-MO and DTPA-BT-F, their PL spectra in THF/water mixtures with different water fractions (f_w) were measured (Fig. S13–S15, ESI†). The relative PL intensities (I/I_0) are shown in Fig. 1C. Owing to the TICT effect in all molecules, their PL intensities gradually decreased when f_w was increased from 0% to ~50%.[39] After that, when more water was added to form the aggregation, much enhanced PL intensities were obtained for all molecules. In particular, even a 16-fold increase was achieved in DTPA-BT-F from pure THF solution to the mixture with a f_w of 90%, indicating its impressive AIE feature.

Notably, when these molecules in THF/water mixtures (f_w = 60%) were stored for a while, nano-precipitation occurred in all cases. Then, time-dependent PL spectra were used to monitor this process (Fig. S16–S18, ESI†). As displayed, a significantly enhanced emission intensity can be observed even by the naked eye. This probably results from the assembled nanoaggregates with closed packing, which gave rise to restricted molecular motions and finally strengthened the brightness. More importantly, in addition to the enhanced brightness, an obvious blue-shifted emission was also observed in the case of DTPA-BT-F (Fig. 1D). This is also similar to other reported studies, which is attributed to the formed crystals caused by the attached fluorine atoms to enhance non-covalent intermolecular interactions.[29,40,41] It should be mentioned that the nano-precipitation here can be controlled by tuning the water fraction or concentration of mixed solutions.[29,31] Also, it is noted that this precipitation is a time-dependent process. Therefore, by using an appropriate water fraction (f_w = 60%), concentration ($[c] = \sim 10^{-5}$ M) and aging time, these time-dependent PL spectra here can be well recorded. Additionally, to verify the reproducibility of the photo-physical studies in our case, three parallel experiments in the THF/water mixture ($[c] = 2 \times 10^{-5}$ M, f_w = 60%) by using DTPA-BT-F were further conducted here, where an enhanced fluorescence intensity and obvious blue-shifted emission could be observed for all cases over 150 min. What's more, plots of I/I_0 values and maximum emission wavelengths for these three cases at different times are also provided with the corresponding error bar (Fig. S19, ESI†). The results demonstrated that DTPA-BT-F may be a promising candidate for the preparation of high quality AIE nanocrystals for biological research. On the other hand, to further confirm the nano-precipitation, the colloidal size and PDI values for DTPA-BT-F in this process were also investigated by dynamic light scattering (DLS). As displayed, during the whole process, the slightly increased hydration diameter is only 300–400 nm with the PDI values of ~0.3, indicating the occurred nano-precipitation here (Fig. S19, ESI†). However, it is noteworthy that if the mixtures were stored for several more hours or days, large-sized precipitation may finally occur. This will be discussed later.

After that, PL spectra of DTPA-BT-H, DTPA-BT-MO and DTPA-BT-F in solids were then measured (Fig. 1E). In the case of DTPA-BT-H and DTPA-BT-MO, emission spectra in solids were similar to those in the solution state, while a dramatic hypsochromic shift of 100 nm was found in DTPA-BT-F, which is probably generated from its intensive crystalline features in solids.[40–42] Subsequently, the absolute PLQYs (Φ) of these AIEgens were investigated (Table S1, ESI†). Here, PLQY values of 24.06%, 36.26% and 4.03% were recorded in solution for DTPA-BT-H, DTPA-BT-MO and DTPA-BT-F, respectively. However, totally different values were observed in their corresponding solid states. Particularly, a maximum PLQY value of 36.49% was obtained in DTPA-BT-F, which was consistent with its AIE characteristics. The high brightness here indicated that DTPA-BT-F may well meet the requirements of STED nanoscopy.[12,16] In addition, transient decay spectra of DTPA-BT-H, DTPA-BT-MO and DTPA-BT-F in both solution and solids were investigated (Fig. S20–S22, ESI†). The corresponding data, including lifetimes (τ), radiative decay rates (k_r), and non-radiative decay rates (k_{nr}), are also summarized (Table S1, ESI†).[43] The large k_{nr} value (93.17×10^7 s^{-1}) in solution and also the large k_r value (8.65×10^7 s^{-1}) in solids for DTPA-BT-F partly explained its entirely distinct PLQY values in the two different states.

To further understand the luminescence performances of DTPA-BT-H, DTPA-BT-MO and DTPA-BT-F in aggregates, powder X-ray diffraction (PXRD) analysis was then conducted (Fig. S23, ESI†). As displayed, all the pristine samples here were microcrystalline in nature with sharp reflections. It was noted that for DTPA-BT-F, much intense peaks appeared. Furthermore, the large 2θ value of 6.46° in this case also corresponded to the intensive molecular packing and strong restriction on molecular-motion, thus contributing to the high luminescence performance.[44] This also verified the fact that nano-precipitation of DTPA-BT-F can be easily achieved in the THF/water mixtures. We then want to further confirm this

conclusion from another view. If the compound is packed orderly in crystals, when it is ground into an amorphous state, red-shifted and decreased emission should be observed.[40,45] Therefore, as a proof-of-concept, the pristine powders of DTPA-BT-H, DTPA-BT-MO and DTPA-BT-F were vigorously ground (Fig. S24–S26, ESI†) and their corresponding PL spectra before/after grinding were also measured (Fig. 1F–H). As observed, red-shifted emission with a slightly decreased intensity was observed in DTPA-BT-H, whereas blue-shifted emission occurred for DTPA-BT-MO. This blue shift here is probably caused by the further twisted molecular conformation in the ground form caused by the external grinding force.[46] It is interesting to note that a significantly decreased emission occurred in the ground DTPA-BT-F, together with an obvious red-shift of 25 nm in λ_{em}. From the results, it is clear that by attaching the fluorine atom to the molecular backbone, the crystalline ability was significantly improved in DTPA-BT-F, thus leading to its impressive AIE characteristics and also high PLQY in solids. This also inspired us to prepare the DTPA-BT-F-based NCs for biological research, such as super-resolution imaging.

As we mentioned above, several strategies to fabricate AIE NCs have been reported.[29,31–33] For instance, by tuning the solvents and their ratios, NCs can be obtained within several days (Fig. 2A). However, due to the impressive crystalline ability of DTPA-BT-F, we also want to prepare its corresponding NCs in a much fast and facile way, such as by using the nanoprecipitation method (Fig. 2B).[47] The preparation processes by using these two methods were compared, and the detailed procedures are included in the experimental section. Transmission electron microscopy (TEM) and selected area electron diffraction (SAED) analysis were adopted here to monitor and investigate the morphology of formed aggregates. For the first case in the THF/water mixture (Fig. 2A), the time-dependent morphologies and the assembled process are displayed (Fig. 2C–J). Initially, amorphous micron-sized aggregates were captured as a result of the rapid precipitation (Fig. 2C and D). Then, as time went by, the turbid solution may reach kinetic stability, where metastable nanoclusters were formed and dispersed (Fig. 2E and F).[29] Afterwards, the nanoclusters were probably transformed into thermodynamically favourable NPs (Fig. 2G–I),[48] and finally, when the mixture was stored for 6 d, nano-crystalline features in the obtained NPs appeared (Fig. 2J). The inset SAED images (Fig. 2J), as well as the observed multiple crystal lattice distances of 2.0 Å and 3.1 Å (Fig. 2L), further demonstrated the successful preparation of DTPA-BT-F-based NCs. The fluorescence images in this process were also captured under a UV lamp (Fig. 2K), indicating the formation of highly emissive NCs.[29] Although NCs can be prepared by using the first method, it is a time-consuming process, and some large sized precipitates can also be observed (Fig. S27, ESI†), which is probably not suitable for cellular imaging. Therefore, the nanoprecipitation method may be a better choice. To our surprise, DTPA-BT-H and DTPA-BT-MO just precipitated as the amorphous NPs (Fig. 2M and N), but for DTPA-BT-F, both the SAED pattern (Fig. 2O) and high-resolution TEM (HRTEM) image (Fig. 2P) confirmed the nano-crystalline characteristics. It should be mentioned that although this nanoprecipitation is a kinetically controlled process (30 s), DTPA-BT-F NCs can still be produced as a result of the much strengthened intermolecular actions by fluorine atoms, which we think is the key point to fabricate nanocrystals by using the twisted AIE-active molecules. What's more, the prepared NPs (DTPA-BT-H and DTPA-BT-MO) and NCs (DTPA-BT-F) were further studied by DLS (Fig. S28, ESI†). Similar to DTPA-BT-H- and DTPA-BT-MO-based NPs, a hydrodynamic diameter of ~153 nm was obtained in DTPA-BT-F NCs with a PDI value of 0.21. In addition to the monodisperse properties, DTPA-BT-F NCs also exhibited a good colloidal stability. To further demonstrate their stability, our prepared nanocrystals dispersed in water and cell growth media, including the freshly-prepared ones and the room temperature-stored ones (3 d), were also characterized by TEM (Fig. S29, ESI†). The results indicated that nano-spheres with similar diameters can be obtained here together with the crystalline properties by SAED for all samples. These results implied that although the kinetically controlled nanoprecipitation method was employed here, DTPA-BT-F-based NCs were stable enough to meet the requirements in cell imaging.

To gain a deeper insight into the NC formation in DTPA-BT-F, theoretical calculations were carried out. Molecular geometries of DTPA-BT-H, DTPA-BT-MO and DTPA-BT-F were firstly optimized by density functional theory (DFT) calculations *via* the Gaussian 09 program. As depicted in Fig. 3A–C, twisted conformations were observed in all the molecules due to the

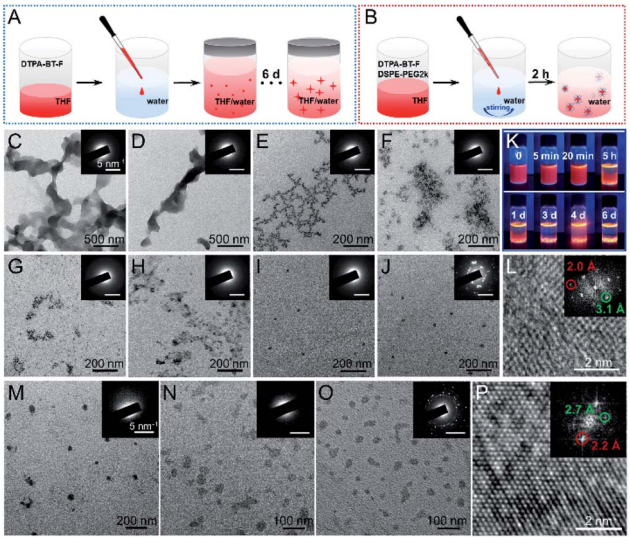

Fig. 2 Schematic illustration of the preparation of nanocrystals by a previously reported method (A) and the nanoprecipitation method (B); TEM images of DTPA-BT-F in the THF/water mixture stored for 0 min, 5 min, 20 min, 5 h, 1 d, 3 d, 4 d, and 6 d (C–J, the insets are their corresponding SAED patterns); the fluorescence images of the DTPA-BT-F contained mixture from C–J (K); HRTEM image of the DTPA-BT-F nanocrystal in J (L, the inset is the Fourier transformation pattern); TEM images of DTPA-BT-H NPs (M), DTPA-BT-MO NPs (N), and DTPA-BT-F NCs (O) prepared by the nanoprecipitation method (the insets are their corresponding SAED patterns); the HRTEM image of DTPA-BT-F NCs in O (P, the inset is the Fourier transformation pattern).

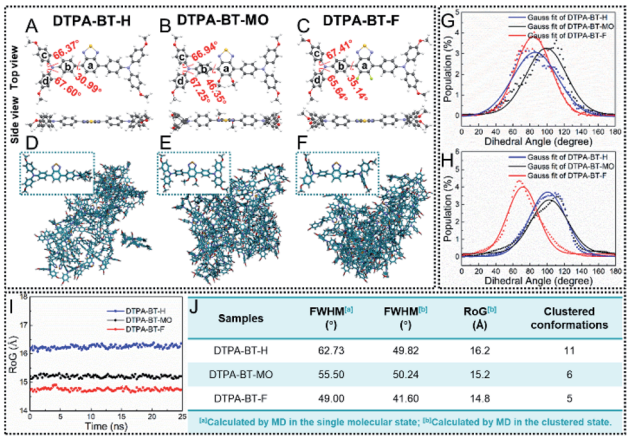

Fig. 3 Optimized geometries of DTPA-BT-H (A), DTPA-BT-MO (B) and DTPA-BT-F (C) *via* DFT (including the top view and side view); snapshots of the geometries of DTPA-BT-H (D), DTPA-BT-MO (E) and DTPA-BT-F (F) in a single molecule and aggregates obtained *via* MD simulations; dihedral angle distributions between phenyl rings *b* and *d* for all molecules in the single molecular state (G) and aggregated state (H); RoG values of DTPA-BT-H, DTPA-BT-MO and DTPA-BT-F in aggregates (I); The corresponding data from G–I and the cluster analysis (J).

propeller-shaped TPA, which can efficiently hamper the molecular π–π stacking and thus induce an enhanced emission efficiency in aggregated states.[49] Resulting from the steric hindrance of methoxy and fluorine groups, DTPA-BT-MO and DTPA-BT-F possessed larger dihedral angles of 46.35° and 35.14° between phenyl rings *a* and *b*, respectively. The electron distribution was also calculated (Fig. S30, ESI†). Similar to the typical D–A structured molecules, the highest occupied molecular orbital (HOMO) was distributed over the entire backbone and the lowest unoccupied molecular orbital (LUMO) was mainly localized on the BT acceptor. It revealed a strong pull–push effect in all these molecules and gave the explanation for their remarkable solvatochromic properties (Fig. S11 and S12, ESI†).[50] Moreover, electrostatic potential (ESP) distribution of these molecules was then simulated (Fig. S31, ESI†). In spite of the similar molecular backbone, DTPA-BT-F obviously displayed electron-withdrawing features and the corresponding negative values in ESP,[51] implying the possibility of enhanced molecular interactions.

On the other hand, we also used molecular dynamics (MD) simulations to investigate their conformations in the single molecular state and aggregated state in water (Fig. 3D–F). The snapshots from MD simulations illustrated that by tuning the substitution in the molecular backbone, the packing manners in aggregates for these molecules can be changed: DTPA-BT-H and DTPA-BT-MO exhibited obvious loose packing, while DTPA-BT-F showed a robust tendency to tightly aggregate. This was also well in line with the fact that DTPA-BT-F NCs could be prepared by a facile nanoprecipitation method. To look into the packing manner in detail, the dihedral angle distributions of DTPA-BT-H, DTPA-BT-MO and DTPA-BT-F were collected to give the corresponding FWHM values between different phenyl rings (*a* and *b*: Fig. S32, ESI; † *b*–*d*: Fig. 3G and H). As we can see, for phenyl rings *b* and *d* in all the molecules, much broad dihedral angle distributions (20–160°) were observed in the single molecular state. However, when molecules were clustered, these distributions became significantly narrow with much decreased FWHMs (Fig. 3J). This also corresponded to a transition from the freely rotating random state to the restricted aggregated state.[52] It's worth noting that DTPA-BT-F had the smallest FWHM value (41.60°) in the aggregated state, revealing its enhanced packing characteristics. The same conclusion can be drawn from the estimation of the radius of gyration (RoG) values (Fig. 3I), where the lowest RoG value of DTPA-BT-F (14.8 Å) definitely manifested its rigid structures and intensive aggregation tendency.[53] Also, it is proposed that if the molecules packed orderly in the aggregates, such as DTPA-BT-F-based NCs, fewer conformations should be captured. Based on this consideration, the different molecular conformations for these molecules in aggregates were recorded and counted by using an AMBER18 package (Fig. S33–S35, ESI†).[54] The cluster analysis indicated that only 5 clusters existed in DTPA-BT-F (Fig. 3J), showing the best uniformity among these three molecules. Associated with the nano-crystalline structures of DTPA-BT-F (Fig. 2O and P), we could claim that DTPA-BT-F has an intensive trend to stack in a regular manner, thus leading to ordered NCs within a short time.

The photo-physical properties of prepared nanoparticles for DTPA-BT-H and DTPA-BT-MO as well as nanocrystals for DTPA-BT-F were then studied. Firstly, the UV-vis absorption and PL spectra were recorded (Fig. S36 and 37, ESI†), where an ICT absorption of 375–575 nm and a deep-red emission covering from 550–850 nm appeared. Subsequently, we measured PLQYs, and summarized the corresponding ε as well as fluorescence brightness (L) to further understand their fluorescence properties (Table S2, ESI†). Interestingly, the PLQY value of DTPA-BT-F nanocrystals was significantly increased by up to 6.7 times compared to that in the solution state, while the other two nanoparticles did not show any advantages. Then, to further understand the fluorescence properties of DTPA-BT-F, its PLQY values in amorphous powders, crystals (obtained in the THF/hexane mixture), and nanocrystals were also measured, which were recorded to be 20.46%, 45.93% and 27.06%, respectively. It is understandable that DTPA-BT-F in crystals exhibited the highest PLQY value. However, a much higher PLQY value for DTPA-BT-F-based nanocrystals was achieved than that for amorphous powders due to its ordered molecular structures and also restriction in crystalline nano-systems. On the other hand, the photo-stable SiR for STED nanoscopy is also included and compared here.[55] It is interesting that although SiR exhibited impressive emission signals with a PLQY of 36.79% in the solution state, an inferior performance with quenched emission was observed in the aggregated thin film (PLQY = 0.14%). However, in the case of DTPA-BT-F, much higher PLQY values in amorphous powders, crystals, and nanocrystals were obtained than that in solution. The fluorescence images under a UV lamp also indicated much higher brightness for DTPA-BT-F than that in SiR in aggregated states (Fig. S38, ESI†). It is also noted that an extinction coefficient of 13.1×10^3 M^{-1} cm^{-1} and brightness of up to 3.54×10^3 M^{-1} cm^{-1} were also obtained in

DTPA-BT-F NCs (Table S2, ESI†), which are much higher than those of the other two NPs. This indicated the outstanding luminescence performance of DTPA-BT-F NCs.[56] It should be mentioned that fluorescence dyes in aggregated states may play important roles in biological imaging. Therefore, according to the above-mentioned results, it is anticipated that the solid-emissive DTPA-BT-F here can well enrich the toolbox of fluorescence dyes for super-resolution imaging *via* STED nanoscopy, thus providing a new strategy to gain insight into organelle-related biological research.

On the other hand, the photo-bleaching resistance and pH-stability of DTPA-BT-F NCs were investigated next. No signal loss was observed here even when irradiated by a xenon lamp for 1 h (Fig. S39, ESI†). In addition, it is observed that under the irradiation of a high power white laser (200 mW), a much higher photo-bleaching resistance can also be obtained in DTPA-BT-F NCs than that for the commercially photo-stable dye of SiR (Fig. S40, ESI†). Also, similar absorption and PL spectra of DTPA-BT-F NCs dispersed in PBS solutions with different pH values (5.0, 6.5, 7.4 and 8.0) were recorded (Fig. S41, ESI†), indicating their much stable photo-physical properties. After that, the cytotoxicity of DTPA-BT-F NCs was then evaluated by using a Cell Counting Kit-8 (CCK-8) assay (Fig. S42 and S43, ESI†). The viability of both HeLa cells and L02 cells remained over 88% after 24 h incubation with DTPA-BT-F NCs (Fig. S42, ESI†), and a high viability of 87% was also achieved when exposed to light irradiation (Fig. S43, ESI†), indicating the good biocompatibility of DTPA-BT-F NCs. In addition to cell viability, effects of DTPA-BT-F NCs on HeLa cells, such as on the pH of lysosomes, were also investigated (Fig. 4A and B). Here, a commercial lysosome-stained probe of LysoSensor Green DND-189, which exhibited an obvious pH-dependent change of fluorescence intensity in cells, was used.[57] In contrast to the untreated HeLa cells, DTPA-BT-F NC-stained HeLa cells displayed a similar fluorescence intensity from LysoSensor Green DND-189 (Fig. S44, ESI†), also revealing the good biocompatibility of DTPA-BT-F NCs as imaging agents.

Cellular imaging was then conducted, and the uptake of DTPA-BT-F NCs by HeLa cells was investigated by a co-localization experiment with LysoTracker Green DND-26, which is a typical and commercialized LysoTracker. As can be seen, these two probes displayed highly overlapped fluorescence signals (Fig. S45, ESI†). Their co-localization rate was determined by using the following equation:

$$\text{Co-localization rate} = \frac{\text{Co-localization area}}{\text{DTPA-BT-F NCs channel area}}$$

via Leica LAS co-localization software.[58] This calculated value reached 91.16% with a corresponding Pearson coefficient of 87.60%, from which we proposed that DTPA-BT-F NCs were probably ingested into cells by endocytosis.[59] To well understand the cellular uptake of DTPA-BT-F NCs, several experiments were further conducted (Fig. 4C–S). Firstly, the treatment at low temperature (4 °C) dramatically decreased the fluorescence intensity in cells (Fig. 4C, D and S46, ESI†), implying that the cellular uptake of DTPA-BT-F NCs was an active (energy-dependent) process.[60] Meanwhile, other biochemical inhibitors, such as NH_4Cl, chlorpromazine (CPZ), genistein and amiloride were also co-cultured with HeLa cells for further study. As displayed, fluorescence signals for cells treated with NH_4Cl decreased significantly (Fig. 4H–J and S47, ESI†), suggesting that the entry of DTPA-BT-F NCs into cells is through the acidic endocytic pathway.[61] Furthermore, for the cases of CPZ and genistein, decreased fluorescence signals were observed (Fig. 4K–P and S47, ESI†), implying the synergistically clathrin-mediated and caveolae-mediated endocytosis here for DTPA-BT-F NC.[61,62] The inhibition of macropinocytosis by amiloride did not affect the internalization of DTPA-BT-F NCs (Fig. 4Q–S and S47, ESI†), revealing that the entry mechanism of DTPA-BT-F NCs is macropinocytosis-independent.[63] In addition to DTPA-BT-F-based nanocrystals, DTPA-BT-H NPs and DTPA-BT-MO NPs also exhibited good biocompatibility in the cell viability test (Fig. S48, ESI†), enabling cellular imaging in both fixed cells and live cells (Fig. S49, ESI†). However, although fluorescence signals can be observed in all the cases, DTPA-BT-F NCs exhibited the highest PLQY value and brightness, so it was preferred to be the promising candidate for super-resolution imaging by STED nanoscopy.

As we mentioned, for STED agents, the anti-photo-bleaching ability is considered as one of the critical benchmarks. Herein, the intracellular photo-stability of DTPA-BT-F NCs was then studied and compared with those of the commercial lysosome-specific probe of LysoTracker Green DND-26, and cytoskeleton-targeting probes of FITC-labeled and Alexa Fluor488-labeled phalloidin (Fig. S50–S52, ESI†). Firstly, in contrast to the

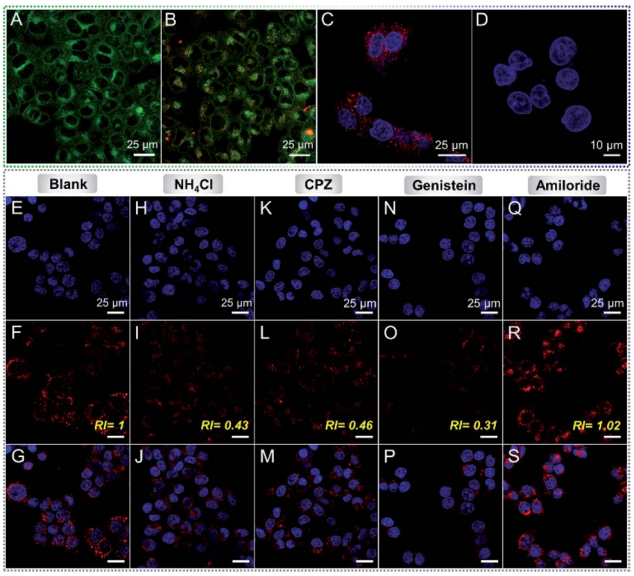

Fig. 4 Fluorescence images of HeLa cells stained with LysoSensor Green DND-189 (green) when treated without (A) or with DTPA-BT-F NCs (red, B) *via* CLSM; fluorescence images of HeLa cells stained with DAPI (blue) and DTPA-BT-F NCs (red) incubated at 37 °C (C) or 4 °C (D) *via* CLSM; fluorescence images of fixed HeLa cells stained with DAPI (blue) and DTPA-BT-F NCs (red) treated without (E–G) or with NH_4Cl (10 mM, H–J), CPZ (50 μM, K–M), genistein (150 μM, N–P) and amiloride (100 μM, Q–S). The inset values are the relative fluorescence intensity (RI) by DTPA-BT-F NCs.

decreased fluorescence signals of LysoTracker Green DND-26, an almost unchanged emission intensity was observed in the case of DTPA-BT-F NCs (Fig. S50, ESI†). Then, during the irradiation by the STED beam (600 mW, 25 min), fluorescence of DTPA-BT-F NCs still remained at about 86%, whereas that of FITC-phalloidin and Alexa Fluor488-phalloidin was almost totally quenched. This further indicated a superior photo-stability of DTPA-BT-F NCs, which was crucial to the long-term tracking in cells (Fig. S51 and S52, ESI†). Accordingly, we infer that the red-emissive DTPA-BT-F NCs with high brightness, a large Stokes' shift of 175 nm (5668 cm^{-1}), outstanding photo-stability and biocompatibility, could be effectively utilized as a STED imaging agent for in-depth exploration in lysosome-related biological research.

After that, DAPI (a nucleus-targeting probe; E_x/E_m 405/408–473 nm), FITC-phalloidin (E_x/E_m 495/500–550 nm), Alexa Fluor488-phalloidin (E_x/E_m 490/495–550 nm) and DTPA-BT-F NCs (E_x/E_m 470/599–740 nm) were then stained in fixed HeLa cells for super-resolution imaging *via* STED nanoscopy (Fig. 5A and S53, ESI†). Taking their emission spectra into account, the STED beams of 592 nm (120 mW), 592 nm (96 mW) and 775 nm (96 mW) were used here for FITC-phalloidin, Alexa Fluor488-phalloidin and DTPA-BT-F NCs, respectively. It is noted that all the images captured by STED nanoscopy were processed on Huygens deconvolution software. As depicted, for both FITC- and Alexa Flour488-phalloidin, the imaging resolution in the cells was partly improved in the STED mode compared to that in the confocal mode (CLSM), giving the FWHM values of 562 nm and 269 nm, respectively (Fig. 5A–D and S53, ESI†), whereas in the case of DTPA-BT-F NCs, the FWHM values substantially decreased from 548 nm to 107 nm *via* STED nanoscopy. Furthermore, the obviously reduced size in captured lysosomes (identified with arrows; ROI 2, Fig. 5E–G) also directly demonstrated that the red-emissive NCs were feasible for practical STED imaging.

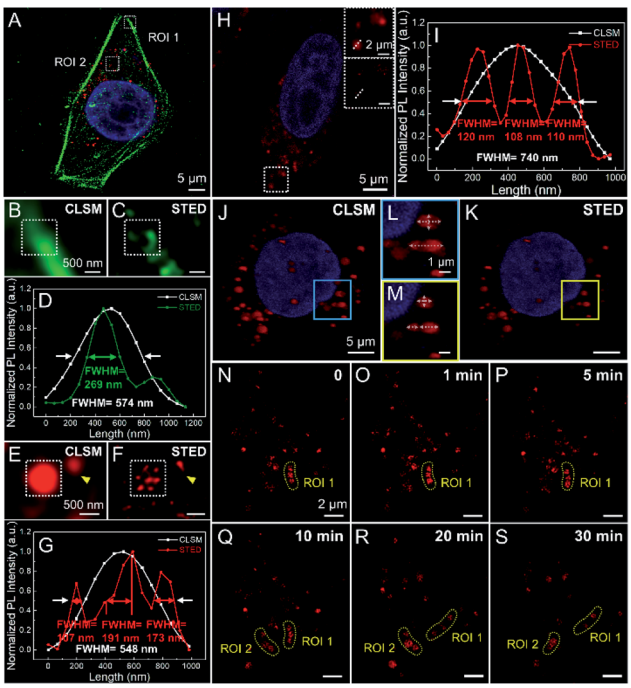

Fig. 5 Fluorescence image of the fixed HeLa cell co-stained with DAPI (blue), Alexa Fluor488-phalloidin (green; depleted by a 592 nm STED laser, 96 mW) and DTPA-BT-F NCs (red; depleted by a 775 nm STED laser, 96 mW) *via* STED nanoscopy (A); magnified fluorescence images by CLSM (B and E), STED nanoscopy (C and F), and their corresponding PL intensity curves (D and G) in ROI 1 (Alexa Fluor488-phalloidin, B–D) and ROI 2 (DTPA-BT-F NCs, E–G) in A; CLSM image of the live HeLa cell stained with Hoechst 33342 (blue) and DTPA-BT-F NCs (red) (H, the insets are the magnified fluorescence images taken in the CLSM and STED mode), and the corresponding PL intensity curves along the dashed line across the lysosome (I); 3D reconstructed images of the live HeLa cell by CLSM (J), STED nanoscopy (K), and their enlarged views (L and M); dynamic movements of lysosomes in HeLa cells captured by STED nanoscopy (N–S). All the STED images are processed on Huygens deconvolution software.

On another aspect, we also investigated the STED efficiency of DTPA-BT-F NCs in fixed HeLa cells by changing the depletion laser power. When the depletion power of the STED beam was increased from 24 mW to 96 mW, the fluorescence intensity decreased accordingly, and some large blurred spots were discriminated into several discrete ones, along with the gradually reduced FWHMs (Fig. S54, ESI†). The corresponding fluorescence intensity (Fig. S55, ESI†) and theoretical lateral resolutions (Fig. S56, ESI†) in DTPA-BT-F NC-stained cells at different powers were obtained. As can be seen, the depletion efficiency of DTPA-BT-F NCs reached up to 72% when the STED beam power is ~96 mW. Meanwhile, an average saturation laser power (P_{sat}) of only 33.1 mW was also obtained in our case, suggesting that DTPA-BT-F NCs could achieve superior resolutions under a much lower STED power, which was desirable for live cell imaging and also long-time tracking in biological research.

Considering the high brightness and depletion efficiency of DTPA-BT-F NCs, we then conducted super-resolution imaging of live HeLa cells under a moderate power of 36 mW. Similar to that in fixed cells, the blurred spots in CLSM can be discriminated into the corresponding detailed structures in the STED mode (Fig. 5H), leading to significantly decreased FWHM values (108 nm, Fig. 5I). Successively, 3D reconstructed cell imaging *via* DTPA-BT-F NCs by CLSM (Fig. 5J) and STED nanoscopy (Fig. 5K) was also performed here. Their corresponding cellular imaging in the 2D view is also listed as a control (Fig. S57, ESI†). In contrast to the 3D confocal image, a single lysosome was observed to be considerably smaller in volume in the 3D-STED mode (Fig. 5L and M). Meanwhile, some adherent and fuzzy lysosomes can be distinguished (dotted arrows). Therefore, it can be concluded that DTPA-BT-F NC-assisted STED imaging not only achieved ultra-high resolution in the two-dimensional view, but also provided more detailed structures in 3D cells.

In view of both outstanding photo-stability and superior imaging resolution of DTPA-BT-F NC-stained cells, we were encouraged to carry out the real-time monitoring and dynamic tracking of lysosomes in live cells *via* STED nanoscopy. After being stained with DTPA-BT-F NCs, the continuous dynamic movements of lysosomes were readily recorded by STED nanoscopy, providing their subtle morphological changes at a superior resolution (Fig. S58, ESI†). This dynamic tracking process

can also be confirmed by the change of corresponding FWHM values. Moreover, the lysosomal contact and dispersion can also be distinguished by changing their size and spatial distribution (Fig. 5N–S). For instance, the adjacent lysosomes in ROI 1 were inactive initially (Fig. 5N–Q), whereas after 20 min, they were gradually dispersed (Fig. 5R and S), probably responding to some intracellular signals.[64] In another case, lysosomes can be resolved to get closer, and finally come into contact with each other (ROI 2). These results prove that DTPA-BT-F NCs hold great potential in biological research with superior resolution, such as lysosome-specific imaging and dynamic monitoring at the nanoscale.

Notably, similar to our previous work,[19] DTPA-BT-F also has a symmetrical D–A–D architecture,[65] and thus it is proposed to also possess two-photon absorption and imaging properties. Therefore, to explore its potential application in two-photon fluorescence (TPF) imaging, DTPA-BT-F NC-stained HeLa cells were also captured by TPF microscopy. This was firstly photo-excited by a varied wavelength from 820 to 1030 nm, and the corresponding emission intensity under different wavelengths was also plotted (Fig. S59, ESI†). As observed, two-photon imaging with high brightness in HeLa cells was achieved when excited at 830 nm, indicating that DTPA-BT-F NCs may also be used for TPF imaging. On the other hand, as our prepared nanocrystals exhibited high brightness, great potential for *in vivo* imaging is also expected by extending their emission wavelength to the near infrared (NIR) region.

Conclusions

In summary, AIE-active DTPA-BT-F with deep-red emission and a high PLQY in solids was synthesized. Benefiting from its enhanced intermolecular actions, DTPA-BT-F exhibited intensive crystalline features, thus leading to facilely prepared nanocrystals by nanoprecipitation. Moreover, highly emissive features, good photo-stability, and excellent biocompatibility were observed in DTPA-BT-F NCs, which were finally applied in lysosome-specific super-resolution imaging *via* STED nanoscopy. The results indicated that the detailed structures of lysosomes at a superior resolution can be captured in both fixed and live cells, even in the reconstructed 3D view. Besides, dynamic monitoring, such as lysosomal contact, can also be achieved by STED nanoscopy to gain insight into organelle-related biological research.

Experimental section

Chemicals and characterization

All chemicals and reagents were commercially available and used as received without further purification. ^{1}H and ^{13}C NMR spectra were recorded on a Bruker Advance III HD 600 MHz spectrometer by using chloroform-*d* as a solvent and tetramethylsilane (TMS, $\delta = 0$ ppm) as an internal reference. High-resolution mass spectra (HR-MS) were obtained on a WATERS I-Class VION IMS QTof in the ESI mode. The UV-vis absorption spectra were recorded by using a PE Lambda950 spectrophotometer. The photoluminescence spectra, lifetime and absolute PLQYs were obtained on a FLS980 transient steady-state fluorescence spectrometer from Edinburgh Instruments by using a Red PMT detector. The wide angle X-ray diffraction (WAXD) measurements were carried out on a Bruker D8 Advance. Dynamic light scattering (DLS) was measured by using a Malvern Zetasizer Nano ZS90. Transmission electron microscopy (TEM) micrographs and selected area electron diffraction (SAED) patterns were collected on a JEOL-2100 electron microscope. The size stability by TEM of DTPA-BT-F NCs in water and cell growth media was captured *via* a FEI Talos F200C. The luminescent photos were taken under the irradiation of a hand-held UV lamp. Confocal images and super-resolution images were captured by using a TCS SP8 STED 3X confocal laser scanning microscope from Leica (Pulse STED, 80 MHz, 12.5 ns; NA = 1.4). All the STED images are processed on Huygens deconvolution software.

Density functional theory (DFT) calculations and molecular dynamics (MD) simulation

Geometry and atomic charge parameters of each molecule (DTPA-BT-H, DTPA-BT-MO and DTPA-BT-F) in a single molecule were obtained by using the Gaussian 09 package at B3LYP/6-31G** level 3.[53,66–68] The original configuration of each molecule in aggregated states was obtained by randomly placing 40 optimized molecules in a 8.0 × 8.0 × 8.0 nm cubic box, and further refined by the 25.0 ns MD simulations by using the Amber18 and GAFF2 force field.[69] An isothermal, isobaric (NPT) ensemble was applied at a constant pressure (1 atm) and 298 K with periodic boundary conditions. The cut-off distances for the electrostatic and van der Waals interactions were set at 1.2 nm. Free dynamics were performed by using a 2.0 fs time step, and coordinates were collected every 10.0 ps. Cpptraj was used to analyze the collected MD snapshots.

Preparation of AIE nanocrystals

Two methods were employed here to prepare the AIE nanocrystals. In the first method, 2.4 mL of water was quickly injected into a THF solution of DTPA-BT-F (0.4 μmol) in a tube with a certain water fraction (f_w = 60%). The tube was then tightly covered to prevent organic solvent evaporation and stored at room temperature until the crystallization was completed (6 days). The process of crystal growth was monitored by TEM. On the other hand, nanoprecipitation was also used to prepare the corresponding nanocrystals. DTPA-BT-F (0.1 mg) and DSPE–PEG2k (0.2 mg) were dissolved in THF (0.1 mL). Then, the THF solution was quickly injected into 5 mL of ultrapure water under stirring for 30 s. THF was then removed by simple evaporation under a fume hood within 2 h.

Cell viability assay

To study the toxicities of DTPA-BT-H NPs, DTPA-BT-MO NPs and DTPA-BT-F NCs in HeLa cells or L02 cells, a Cell Counting Kit-8 (CCK-8) assay was employed. The cells were cultured in Dulbecco's modified eagle medium (DMEM) solution at 37 °C in a humidified atmosphere containing 5% CO_2. They were then seeded in 96-well plates with a density of 10^4 cells per well. The medium was then replaced with 0 (control), 10, 20, 50 and 100

μg mL^{-1} of NP or NC suspension in the DMEM solution. After incubation for 24 h, the absorption of the corresponding NP or NC-stained cells was measured at 450 nm as a blank control to avoid their influence on the CCK-8 assay. Then, the supernatant was removed, followed by the addition of a freshly prepared CCK-8 solution (1 mg mL^{-1} in medium, 100 μL per well) into each well. After 4 h incubation, the absorbance of CCK-8 was monitored at 450 nm using a microplate reader. The toxicity test procedure for DTPA-BT-F NCs in HeLa cells under irradiation conditions was similar to the above-mentioned case. The only difference was that after incubation, plates containing the cells with different concentrations of DTPA-BT-F NCs were exposed to white light (400–800 nm; 100 mW cm^{-2}) for 5 min, and another array of plates was kept in the dark as a control.

Cellular imaging *via* CLSM

CLSM imaging of fixed cells. HeLa cells were seeded in glass-bottom dishes with a density of 5×10^4 mL^{-1}. After the adherence of cells, the upper medium was removed. For the co-staining imaging experiments of fixed HeLa cells, DTPA-BT-H NPs, DTPA-BT-MO NPs or DTPA-BT-F NCs (50 μg mL^{-1} in medium) were added to the cells for incubation first. Later, the cells were fixed with cell fixatives within 10 min. 4′,6-diamidino-2-phenylindole (DAPI) (3 min) was used to stain the fixed cells. After washing the cells with PBS three times, a mounting medium was used for cell preservation. The confocal images of DTPA-BT-H NP, DTPA-BT-MO NP or DTPA-BT-F NC stained cells were recorded on a confocal microscope (63× water-immersion objective).

CLSM imaging of live cells. DTPA-BT-H NPs and DTPA-BT-MO NPs dispersed in the medium (50 μg mL^{-1}) were added to the glass-bottom dishes seeded with HeLa cells. 6 h later, the supernatant was removed and the cells were washed three times with PBS. Then, Hoechst 33342 was added to stain the cells for 20 min. After the DMEM solution was supplied, live HeLa cells were imaged by using CLSM microscopy. For the co-localization imaging experiment, the cells were stained with our prepared NPs or NCs (50 μg mL^{-1}, 6 h) followed by labelling with LysoTracker Green DND-26 (50 nM, 2 h). Then, the cells were washed three times with PBS and kept in DMEM for subsequent imaging. To evaluate the effect of DTPA-BT-F NCs on lysosomal pH, a group of cells was stained with DTPA-BT-F NCs (50 μg mL^{-1}, 6 h), while another one was kept as a control. After that, they were labelled with LysoSensor Green DND-189 (1 μM, 1 h). The cells were washed with PBS and kept in DMEM for imaging.

Pathway study of cellular uptake for DPA-BT-F NCs. The effect of temperature on DTPA-BT-F NC uptake was studied by pre-incubating the cells at 4 °C for 3 h and treating them with NCs (50 μg mL^{-1}) for 3 h at 4 °C. To examine the effects of different inhibitors on the internalization of NCs, HeLa cells were pre-incubated for 1 h at 37 °C with NH_4Cl (10 mM), CPZ (50 μM), genistein (150 μM) or amiloride (100 μM). DTPA-BT-F NCs (50 μg mL^{-1}) were then added into the medium containing the inhibitors, and the cells were incubated for 6 h at 37 °C. Then, the cells were washed with PBS, and fixed with cell fixatives for 10 min followed by staining with DAPI.

Super-resolution imaging *via* STED nanoscopy

Imaging of fixed cells. The imaging experiments of DTPA-BT-F NC (50 μg mL^{-1} in medium) stained fixed cells *via* STED nanoscopy were similar to those of CLSM imaging, with the exception that FITC-phalloidin (200 nM, 30 min) or Alexa Fluor488-phalloidin (20 min) was also used to co-stain the fixed cells. STED lasers at 592 nm and 775 nm were adopted for STED images of FITC-/Alexa Fluor488-phalloidin and DTPA-BT-F NCs, respectively (100× oil-immersion objective; pixel resolution: 47 nm × 47 nm; scan speed: 200 Hz; pinhole size: 151.6 μm). All the images captured by STED nanoscopy were processed on Huygens deconvolution software.

Imaging of live cells. DTPA-BT-F NCs dispersed in the medium (50 μg mL^{-1}) were added to glass-bottom dishes seeded with HeLa cells. 6 h later, the supernatant was removed, and the cells were washed three times with PBS. Then, Hoechst 33342 was added to stain the cells for 20 min. Live HeLa cells were supplied and rinsed with the DMEM solution and imaged by using STED microscopy. A 775 nm STED laser was used (100× oil-immersion objective; pixel resolution: 47 nm × 47 nm; scan speed: 200 Hz; pinhole size: 151.6 μm). All the images captured by STED nanoscopy were processed on Huygens deconvolution software.

Data availability

Data for this paper, including the synthesis, structural characterization, PL spectra in solution, transient decay spectra in solution and in solids, XRD patterns in solids, and theoretical calculations, are available at ESI.†

Author contributions

Ruohan Xu: synthesis, characterization, data analysis, and writing – original draft; Dongfeng Dang: design, data analysis, writing – review & editing, and supervision; Zhi Wang: data analysis; Yu Zhou: characterization; Yanzi Xu: data analysis; Yizhen Zhao: theoretical calculations; Xiaochi Wang: synthesis; Zhiwei Yang: theoretical calculations; Lingjie Meng: data analysis and supervision.

Conflicts of interest

There are no conflicts to declare.

Acknowledgements

The authors are thankful for the financial support from the National Natural Science Foundation of China (21975197, 21674085 and 51603165), the Young Talent Fund of University Association for Science and Technology in Shaanxi, China (20180601), the Key Laboratory Construction Program of Xi'an Municipal Bureau of Science and Technology (201805056ZD7CG40), School of Materials Science and Engineering, Jiangsu Engineering Laboratory of Light-Electricity-Heat Energy-Converting Materials and Applications

(GDRGCS2019001) and the Innovation Capability Support Program of Shaanxi (Program No. 2021TD-57). This work was also supported by the Innovation Capability Support Program of Shaanxi (No. 2018PT-28 and 2019PT-05).

References

1 V. Ntziachristos, *Nat. Methods*, 2010, **7**, 603–614.
2 E. E. Hoover and J. A. Squier, *Nat. Photonics*, 2013, **7**, 93–101.
3 Y. Y. Li, Z. C. Cai, S. J. Liu, H. K. Zhang, S. T. H. Wong, J. W. Y. Lam, R. T. K. Kwok, J. Qian and B. Z. Tang, *Nat. Commun.*, 2020, **11**, 1255.
4 S. W. Hell and J. Wichmann, *Opt. Lett.*, 1994, **19**, 780–782.
5 D. F. Dang, H. K. Zhang, Y. Z. Xu, R. H. Xu, Z. Wang, R. T. K. Kwok, J. W. Y. Lam, L. Zhang, L. J. Meng and B. Z. Tang, *ACS Nano*, 2019, **13**, 11863–11873.
6 R. Heintzmann, T. M. Jovin and C. Cremer, *J. Opt. Soc. Am. A*, 2002, **19**, 1599–1609.
7 Y. C. Wong, D. Ysselstein and D. Krainc, *Nature*, 2018, **554**, 382.
8 M. J. Rust, M. Bates and X. W. Zhuang, *Nat. Methods*, 2006, **3**, 793–795.
9 T. Nerreter, S. Letschert, R. Gotz, S. Doose, S. Danhof, H. Einsele, M. Sauer and M. Hudecek, *Nat. Commun.*, 2019, **10**, 3137.
10 N. Ji, *Nat. Methods*, 2017, **14**, 374–380.
11 Y. M. Sigal, R. B. Zhou and X. W. Zhuang, *Science*, 2018, **361**, 880–887.
12 Y. Z. Xu, R. H. Xu, Z. Wang, Y. Zhou, Q. F. Shen, W. C. Ji, D. F. Dang, L. J. Meng and B. Z. Tang, *Chem. Soc. Rev.*, 2021, **50**, 667–690.
13 L. Wang, M. S. Frei, A. Salim and K. Johnsson, *J. Am. Chem. Soc.*, 2019, **141**, 2770–2781.
14 Y. J. Liu, Y. Q. Lu, X. S. Yang, X. L. Zheng, S. H. Wen, F. Wang, X. Vidal, J. B. Zhao, D. M. Liu, Z. G. Zhou, C. S. Ma, J. J. Zhou, J. A. Piper, P. Xi and D. Y. Jin, *Nature*, 2017, **543**, 229.
15 J. Hanne, H. J. Falk, F. Gorlitz, P. Hoyer, J. Engelhardt, S. J. Sahl and S. W. Hell, *Nat. Commun.*, 2015, **6**, 7127.
16 R. H. Xu, Y. Z. Xu, Z. Wang, Y. Zhou, D. F. Dang and L. J. Meng, *Comb. Chem. High Throughput Screening*, 2021, **24**, 1017–1030.
17 A. N. Butkevich, G. Lukinavicius, E. D'Este and S. W. Hell, *J. Am. Chem. Soc.*, 2017, **139**, 12378–12381.
18 X. F. Fang, X. Z. Chen, R. Q. Li, Z. H. Liu, H. B. Chen, Z. Z. Sun, B. Ju, Y. F. Liu, S. X. A. Zhang, D. Ding, Y. J. Sun and C. F. Wu, *Small*, 2017, **13**, 1702128.
19 Y. Z. Xu, H. K. Zhang, N. Zhang, R. H. Xu, Z. Wang, Y. Zhou, Q. F. Shen, D. F. Dang, L. J. Meng and B. Z. Tang, *Mater. Chem. Front.*, 2021, **5**, 1872–1883.
20 C. G. Wang, A. Fukazawa, M. Taki, Y. Sato, T. Higashiyama and S. Yamaguchi, *Angew. Chem.*, 2015, **127**, 15428–15432.
21 C. G. Wang, M. Taki, Y. Sato, A. Fukazawa, T. Higashiyama and S. Yamaguchi, *J. Am. Chem. Soc.*, 2017, **139**, 10374–10381.
22 Y. Y. Wu, H. F. Ruan, R. Zhao, Z. Z. Dong, W. H. Li, X. J. Tang, J. H. Yuan and X. H. Fang, *Adv. Opt. Mater.*, 2018, **6**, 1800333.
23 D. Y. Li, X. Ni, X. Y. Zhang, L. W. Liu, J. L. Qu, D. Ding and J. Qian, *Nano Res.*, 2018, **11**, 6023–6033.
24 Z. Lv, Z. W. Man, H. T. Cui, Z. Z. Xu, H. H. Cao, S. Li, Q. Liao, Q. H. He, L. M. Zheng and H. B. Fu, *Adv. Funct. Mater.*, 2021, **31**, 2009329.
25 Y. Z. Xu, H. K. Zhang, N. Zhang, X. C. Wang, D. F. Dang, X. N. Jing, D. Xi, Y. Hao, B. Z. Tang and L. J. Meng, *ACS Appl. Mater. Interfaces*, 2020, **12**, 6814–6826.
26 D. Y. Li, W. Qin, B. Xu, J. Qian and B. Z. Tang, *Adv. Mater.*, 2017, **29**, 1703643.
27 Z. H. Liu, J. Liu, X. D. Wang, F. X. Mi, D. Wang and C. F. Wu, *Bioconjugate Chem.*, 2020, **31**, 1857–1872.
28 Z. Wang, Y. Zhou, R. Xu, Y. Xu, D. Dang, Q. Shen, L. Meng and B. Z. Tang, *Coord. Chem. Rev.*, 2022, **451**, 214279.
29 S. M. A. Fateminia, Z. M. Wang, C. C. Goh, P. N. Manghnani, W. B. Wu, D. Mao, L. G. Ng, Z. J. Zhao, B. Z. Tang and B. Liu, *Adv. Mater.*, 2017, **29**, 1604100.
30 S. M. A. Fateminia, L. Kacenauskaite, C. J. Zhang, S. M. Kenry, P. N. Manghnani, J. S. Chen, S. D. Xu, F. Hu, B. Xu, B. W. Laursen and B. Liu, *Small*, 2018, **14**, 1803325.
31 Z. Zheng, D. Y. Li, Z. Y. Liu, H. Q. Peng, H. H. Y. Sung, R. T. K. Kwok, I. D. Williams, J. W. Y. Lam, J. Qian and B. Z. Tang, *Adv. Mater.*, 2019, **31**, 1904799.
32 J. Tavakoli, S. Pye, A. Reza, N. Xie, J. Qin, C. L. Raston, B. Z. Tang and Y. H. Tang, *Mater. Chem. Front.*, 2020, **4**, 537–545.
33 K. Q. Chen, R. Y. Zhang, G. G. Li, B. X. Li, Y. Ma, M. Sun, Z. M. Wang and B. Z. Tang, *Mater. Horiz.*, 2020, **7**, 3005–3010.
34 D. F. Dang, D. H. Yu and E. G. Wang, *Adv. Mater.*, 2019, **31**, 1807019.
35 B. C. Schroeder, Z. G. Huang, R. S. Ashraf, J. Smith, P. D'Angelo, S. E. Watkins, T. D. Anthopoulos, J. R. Durrant and I. McCulloch, *Adv. Funct. Mater.*, 2012, **22**, 1663–1670.
36 D. F. Dang, W. C. Chen, R. Q. Yang, W. G. Zhu, W. Mammo and E. G. Wang, *Chem. Commun.*, 2013, **49**, 9335–9337.
37 D. O'Connor, A. Byrne, G. B. Berselli, C. Long and T. E. Keyes, *Analyst*, 2019, **144**, 1608–1621.
38 R. R. Hu, E. Lager, A. Aguilar, J. Z. Liu, J. W. Y. Lam, H. H. Y. Sung, I. D. Williams, Y. C. Zhong, K. S. Wong, E. Pena-Cabrera and B. Z. Tang, *J. Phys. Chem. C*, 2009, **113**, 15845–15853.
39 D. F. Dang, H. X. Liu, J. G. Wang, M. Chen, Y. Liu, H. H. Y. Sung, I. D. Williams, R. T. K. Kwok, J. W. Y. Lam and B. Z. Tang, *Chem. Mater.*, 2018, **30**, 7892–7901.
40 Z. Wu, S. Z. Mo, L. N. Tan, B. Fang, Z. Q. Su, Y. T. Zhang and M. Z. Yin, *Small*, 2018, **14**, 1802524.
41 Q. Q. Li and Z. Li, *Acc. Chem. Res.*, 2020, **53**, 962–973.
42 Y. Q. Dong, J. W. Y. Lam and B. Z. Tang, *J. Phys. Chem. Lett.*, 2015, **6**, 3429–3436.
43 H. Nie, K. Hu, Y. J. Cai, Q. Peng, Z. J. Zhao, R. R. Hu, J. W. Chen, S. J. Su, A. J. Qin and B. Z. Tang, *Mater. Chem. Front.*, 2017, **1**, 1125–1129.
44 Y. J. Xie, Y. W. Ge, Q. Peng, C. G. Li, Q. Q. Li and Z. Li, *Adv. Mater.*, 2017, **29**, 1606829.
45 X. L. Luo, J. N. Li, C. H. Li, L. P. Heng, Y. Q. Dong, Z. P. Liu, Z. S. Bo and B. Z. Tang, *Adv. Mater.*, 2011, **23**, 3261–3265.

46 S. Dineshkumar and I. R. Laskar, *Polym. Chem.*, 2018, **9**, 5123–5132.
47 S. Fery-Forgues, *Nanoscale*, 2013, **5**, 8428–8442.
48 C. Q. Yuan, A. Levin, W. Chen, R. R. Xing, Q. L. Zou, T. W. Herling, P. K. Challa, T. P. J. Knowles and X. H. Yan, *Angew. Chem., Int. Ed.*, 2019, **58**, 18116–18123.
49 T. X. Liu, L. P. Zhu, C. Zhong, G. H. Xie, S. L. Gong, J. F. Fang, D. G. Ma and C. L. Yang, *Adv. Funct. Mater.*, 2017, **27**, 1606384.
50 H. B. Xiao, P. Li, W. Zhang and B. Z. Tang, *Chem. Sci.*, 2016, **7**, 1588–1593.
51 Y. Xu, H. F. Yao, L. J. Ma, L. Hong, J. Y. Li, Q. Liao, Y. F. Zu, J. W. Wang, M. Y. Gao, L. Ye and J. H. Hou, *Angew. Chem., Int. Ed.*, 2020, **59**, 9004–9010.
52 D. Wang, M. M. S. Lee, W. H. Xu, G. G. Shan, X. Y. Zheng, R. T. K. Kwok, J. W. Y. Lam, X. L. Hu and B. Z. Tang, *Angew. Chem., Int. Ed.*, 2019, **58**, 5628–5632.
53 Y. Z. Xu, C. B. Li, R. H. Xu, N. Zhang, Z. Wang, X. N. Jing, Z. W. Yang, D. F. Dang, P. F. Zhang and L. J. Meng, *Chem. Sci.*, 2020, **11**, 8157–8166.
54 Z. W. Yang, Y. Z. Zhao, D. X. Hao, S. L. Ren, X. H. Yuan, L. J. Meng and S. L. Zhang, *J. Biomol. Struct. Dyn.*, 2020, **38**, 1918–1926.
55 N. Wang, Y. Hao, X. Feng, H. Zhu, D. Zhang, T. Wang and X. Cui, *Chin. Chem. Lett.*, 2021, DOI: 10.1016/j.cclet.2021.06.075.
56 J. Qi, X. C. Duan, W. Y. Liu, Y. Li, Y. J. Cai, J. W. Y. Lam, R. T. K. Kwok, D. Ding and B. Z. Tang, *Biomaterials*, 2020, **248**, 120036.
57 X. W. Ma, Y. Y. Wu, S. B. Jin, Y. Tian, X. N. Zhang, Y. L. Zhao, L. Yu and X. J. Liang, *ACS Nano*, 2011, **5**, 8629–8639.
58 Z. G. Yue, W. Wei, P. P. Lv, H. Yue, L. Y. Wang, Z. G. Su and G. H. Ma, *Biomacromolecules*, 2011, **12**, 2440–2446.
59 S. Behzadi, V. Serpooshan, W. Tao, M. A. Hamaly, M. Y. Alkawareek, E. C. Dreaden, D. Brown, A. M. Alkilany, O. C. Farokhzad and M. Mahmoudi, *Chem. Soc. Rev.*, 2017, **46**, 4218–4244.
60 A. Salvati, C. Åberg, T. Santos, J. Varela, P. Pinto, I. Lynch and K. A. Dawson, *Nanomedicine*, 2011, **7**, 818–826.
61 C. J. Guo, Y. Y. Wu, L. S. Yang, X. B. Yang, J. He, S. Mi, K. T. Jia, S. P. Weng, X. Q. Yu and J. G. He, *J. Virol.*, 2012, **86**, 2621–2631.
62 L. M. Wang, Y. Liu, W. Li, X. M. Jiang, Y. L. Ji, X. C. Wu, L. G. Xu, Y. Qiu, K. Zhao, T. T. Wei, Y. F. Li, Y. L. Zhao and C. Y. Chen, *Nano Lett.*, 2011, **11**, 772–780.
63 V. K. Lik, Y. C. Hoay, H. V. Siew, E. Gallon, J. Movellan, H. N. Kia, S. Alpugan, B. L. Hong, F. Dumoulin, M. J. Vicent and Y. C. Lip, *Nanomedicine*, 2017, **13**, 1447–1458.
64 A. Ballabio and J. S. Bonifacino, *Nat. Rev. Mol. Cell Biol.*, 2020, **21**, 101–118.
65 X. Zhou, F. T. Kong, Y. Sun, Y. Huang, X. X. Zhang and R. Ghadari, *Dyes Pigm.*, 2020, **173**, 107954.
66 *Gaussian 09, Revision A.02*, Gaussian Inc., Wallingford CT, USA, 2009.
67 F. Wang, J. Liu, D. Q. Wang, Z. W. Yang, K. Yan and L. J. Meng, *Nanoscale*, 2019, **11**, 15017–15022.
68 D. F. Dang, X. C. Wang, D. Q. Wang, Z. W. Yang, D. X. Hao, Y. Z. Xu, S. L. Zhang and L. J. Meng, *ACS Appl. Nano Mater.*, 2018, **1**, 2324–2331.
69 J. M. Wang, R. M. Wolf, J. W. Caldwell, P. A. Kollman and D. A. Case, *J. Comput. Chem.*, 2004, **25**, 1157–1174.